Influence of Pt particle size and reaction phase on the photocatalytic performances of ultradispersed Pt/TiO2 catalysts for hydrogen evolution

C. Dessal, L. Martinez, C. Maheu, T. Len, F. Morfin, J. Rousset, E. Puzenat, P. Afanasiev, M. Aouine, L. Soler, et al.

Influence of Pt particle size and reaction phase on the photocatalytic performances of ultradispersed Pt/TiO_2 catalysts for hydrogen evolution

C. Dessal,[1a] L. Martínez,[2a] C. Maheu,[1] T. Len,[1] F. Morfin,[1] J.L. Rousset,[1] E. Puzenat,[1] P. Afanasiev,[1] M. Aouine,[1] L. Soler,[2] J. Llorca,[2,*] L. Piccolo[1,*]

[1] *Univ Lyon, Université Claude Bernard - Lyon 1, CNRS, IRCELYON - UMR 5256, 2 Avenue Albert Einstein, F-69626 VILLEURBANNE CEDEX, France. * laurent.piccolo@ircelyon.univ-lyon1.fr*

[2] *Institute of Energy Technologies, Department of Chemical Engineering and Barcelona Research Center in Multiscale Science and Engineering, Universitat Politècnica de Catalunya, EEBE, Eduard Maristany 16, 08019 Barcelona, Spain. * jordi.llorca@upc.edu*

Abstract

Pt/TiO_2 photocatalysts were prepared by incipient wetness impregnation followed by oxidative and/or reductive thermal treatments. By varying the TiO_2 form (commercial P25 and P90, and homemade shape-controlled), the Pt loading (0.2-1 wt% Pt) and the treatment temperature (200-600 °C), it has been possible to tune the Pt cluster size. An increase in the ethanol dehydrogenation rate under ultraviolet irradiation as the Pt cluster average diameter decreases from 17 to 9 Å is suggested by our data. Whereas pre-reduction in H_2 leads to Pt clusters, pre-calcination in air leads to atomically dispersed cationic Pt species. The former are more active and stable than the latter. This conclusion is valid both in gas- and liquid-phase reaction conditions for given TiO_2 type and Pt loading. The activity results are consistent with a recent theoretical work showing that 1 nm is an optimal Pt cluster size for favoring both photoelectron transfer from TiO_2 to Pt and hydrogen coupling on Pt. The best catalytic performance is obtained in gas phase for pre-reduced 0.2 wt% Pt/TiO_2-P90, with an H_2 production rate of 170 mmol h^{-1} g_{cat}^{-1}.

Keywords

Photocatalysis; Hydrogen evolution reaction; Pt/TiO_2; Metal ultradispersion; Size effects

[a] These two authors equally contributed to this work.

1. Introduction

It is urgent to develop alternatives to fossil fuels. Sunlight is a renewable, environment-friendly energy source and hydrogen is one of the most promising solar fuels [1]. Three photocatalytic reactions can produce hydrogen: photocatalytic water splitting [2], photocatalytic dehydrogenation and photocatalytic reforming. The second and the third processes may use biomass-derived alcohols such as methanol or ethanol [3–12].

The reference photocatalytic material, TiO_2 semiconductor, must be supplemented by a co-catalyst to increase the photocatalytic hydrogen evolution reaction (PHER) efficiency. The role of the co-catalyst, which can be a metal [13,14] or a semiconductor [15], is to enhance the charge career separation through the collection of photoelectrons, and thereby avoid electron-hole recombination [13,16,17]. Although noble metals such as Au and Pd -or combinations- have also proven to be efficient [5,6,13,18–20], Pt/TiO_2, with a Pt loading as low as 0.2 wt%, is the most popular system [7,9,16,21].

As metal particle size influences the number and type of active sites, but also the overall electronic structure in the case of small particles (clusters of size < 2 nm) due to quantum size confinement, Pt nanoparticle size is expected to influence the Pt/TiO_2 activity. For example, a Pt cluster size effect in PHER was evidenced in combination with CdS and a triethanolamine/water mixture by Schweinberger *et al.*, with a maximum activity for Pt_{46} clusters [22]. This effect was attributed to the size-dependent electronic properties of the metal clusters with respect to the band edges of the semiconductor. From theoretical calculations, Wang *et al.* predicted 1 nm to be the optimum size for titania-supported Pt particles in PHER, as it fits the requirements for both electron transfer and H-H coupling [23]. In contrast to these findings, from investigations of Pt/TiO_2 catalysts exhibiting single Pt cations, two groups have recently concluded that these atomically dispersed species are more active than metallic Pt nanoparticles for PHER from methanol aqueous solution [24–26].

In this paper, we investigate the photocatalytic dehydrogenation of ethanol in water over a variety of Pt/TiO_2 systems. Two commercial and three homemade shape-controlled titania supports as well as various Pt impregnation post-treatments and two Pt loadings have been employed in combination with thorough pre- and post-reaction analysis of the samples by scanning transmission electron microscopy (STEM) in an image-aberration-corrected microscope. Moreover, we have compared the photocatalytic performances between gas-phase and liquid-phase conditions. Our results suggest that Pt particle size is a key parameter driving PHER, and that nanosized metallic clusters are more active and much more stable under the reaction conditions than single Pt cations.

2. Experimental

2.1. Materials and catalyst preparation

Shape-controlled TiO_2 samples (nanotubes, nanowires and nanobelts) were prepared following literature methods [27,28]. In addition, two commercial TiO_2 materials (Evonik Aeroxide, purity >99.5%) were used in this study, P25 and P90. Table 1 reports the main characteristics of all the considered titania supports.

Table 1. Characteristics of TiO_2 phases

TiO_2 sample	**TiO_2 phases**	**S_{BET} (m^2/g)**
P25	80% anatase, 20% rutile	50
P90	92% anatase, 8% rutile	114
Nanotubes	anatase	274
Nanowires	75% anatase, 25% TiO_2(B)	250
Nanobelts	91% TiO_2(B), 9% anatase	35

S_{BET} denotes the Brunauer-Emmett-Teller surface area, as measured by N_2 adsorption volumetry (Micromeritics ASAP 2020) at -196 °C, with pre-outgassing at 300 °C for 3 h (commercial samples) or 500 °C for 10 h (nanoshaped samples) under secondary vacuum.

Pt/TiO_2 samples were prepared by incipient wetness impregnation with an aqueous solution of $Pt(NH_3)_4(NO_3)_2$ precursor (Sigma-Aldrich, >50%), followed by drying at 60 °C for 4 h and calcination (synthetic air) and/or reduction (pure H_2) treatment (gas flow 30 mL/min, standard temperature 300 °C, heating rate 2 °C/min, plateau 2 h). Pt loadings were measured by inductively coupled plasma - optical emission spectroscopy (ICP-OES Activa from Horiba Jobin Yvon) after the samples were pre-reduced at 450 °C in H_2 flow and dissolved in an acid mixture at 300 °C. The actual Pt loadings corresponding to 0.2 wt% Pt and 1.0 wt% Pt target loadings were 0.15 ± 0.04 wt% and 0.78 ± 0.22 wt%, respectively (see Table 2 in Section 3.1).

2.2. Scanning transmission electron microscopy

The annular-dark-field STEM experiments (ADF-STEM) were performed with a FEI Titan ETEM G2 electron microscope equipped with a Cs image aberration corrector and operated at 300 keV. The extraction voltage, camera length, acceptance angles, STEM resolution and probe current were 4500 V, 245 mm, 29.2-146 °, 0.14 nm and <0.1 nA, respectively. For sample preparation, the powder was crushed and sonicated in ethanol, dropped onto a TEM grid, and dried by a lamp. To avoid contamination during analysis and remove all residual carbon, the samples were Ar plasma-cleaned for 20 s (Plasma Prep 5, GaLa Instrumente). A simple-tilt FEI sample holder and holey carbon-coated

200 mesh Cu grids were used for high-vacuum analyses at RT. No filtering was applied on the STEM images. Particle size histograms were obtained from the analysis of several images with the help of ImageJ software. The average particle diameter was calculated from the mean diameter frequency distribution with the formula: $d = \Sigma n_i d_i / \Sigma n_i$, where n_i is the number of particles with particle diameter d_i in a certain range. The diameter is that of the disk having the same area as the projected STEM image of the object. The error on particle size corresponds to standard deviation.

2.3. Photocatalytic ethanol dehydrogenation

Photocatalysts tests in the gas phase

The photocatalytic tests were performed at RT and atmospheric pressure in a tubular glass photoreactor [29,30]. An argon stream (20 mL/min) was bubbled into a Drechsel bottle containing a liquid mixture of ethanol and water to obtain a gaseous reactant mixture of EtOH:H_2O=1:9 (molar basis), which was directly introduced in the reactor. The UV-light source (from SACOPA, S.A.U.) consisted of four LEDs at 365±5 nm (diameter 18 mm, total power 760 W/m^2) and a synthetic quartz glass cylindrical lens that transmits the light to the photocatalyst. A circular cellulose membrane (Albet, pore size 35-40 µm, density 80 g/m², thickness 180 µm) was impregnated in its central part (disk of 18 mm in diameter) with 1.8 ± 0.2 mg of grinded catalyst dispersed in ethanol through ultrasonication. The membrane was then placed between the glass tubes of the photoreactor, with the side that contains the photocatalyst facing towards the UV-light source. The reactor tubes and the impregnated membrane were sealed using an O-ring, parafilm and a clamp. The photoreactor was connected to a GC (micro gas chromatograph Agilent 490) equipped with MS 5Å, Plot U and Stabilwax columns for a complete analysis of the photoreaction products, which were monitored on-line every 4 minutes. Before the photocatalytic tests, the system was purged with argon for one hour, and the absence of oxygen was checked by GC.

Photocatalysts tests in the liquid phase

The photocatalytic tests were performed in a double-wall semi-batch slurry reactor with 600 rpm stirring. Its temperature was regulated to 20 °C through thermostated water recirculation in the double-wall. The reactor was filled with 50 mg of catalyst dispersed in 50 mL of a mixture of ethanol and distilled water (50:50 vol%). Before irradiation, the system was purged with an argon flow for 30 min. The gases were analyzed by micro GC with thermal conductivity detectors (Agilent 300A equipped with MS 5A, PLOT U, OV-1 and Alumina columns). A 125 W high-pressure mercury polychromatic lamp was used to illuminate the reactor through a 20 cm^2 surface area. The incident photon intensity likely to be absorbed by the photocatalyst was measured with a radiatometer device composed of a spectrometer (Avantes, AvaSpec-2018) coupled with a seven-fiber optics probe (Avantes, FCR-7UV-400-2-ME).

In both gas- and liquid-phase conditions, only H_2 and acetaldehyde were produced. No CO_2, CO or other secondary products were formed, meaning that the only observed reaction was primary ethanol dehydrogenation:

$$C_2H_5OH \rightarrow C_2H_4O + H_2 \qquad (1)$$

The photonic yield writes as follows [31]:

$$PY = \frac{r_{H_2}}{\Phi_{phot}}$$

where r_{H2} is the dihydrogen formation rate and Φ_{phot} is the absorbable photon flux. In order to facilitate comparison of measured *PY* with the literature, we also refer to the apparent quantum yield, which writes as [16,32]:

$$AQY = \frac{2r_{H_2}}{\Phi_{phot}^{tot}}$$

In gas-phase conditions, $\Phi_{phot} = \Phi_{phot}^{tot} = 2120$ µmol/h (diode power 760 W/m², S_{opt} = 2.54 cm², λ = 365 nm). In liquid-phase conditions, the UV lamp is polychromatic with a total photon flux of Φ_{phot}^{tot} = 6600 µmol/h (power 220 W/m², $S_{opt} \approx 20$ cm²). The TiO_2 samples absorbing only in the 290 – 410 nm range (see irradiance spectrum, Fig. S0), the flux of absorbable photons is Φ_{phot} = 1500 µmol/h. Note that in the case of polychromatic irradiation (as in the liquid-phase conditions used here), *PY* and *AQY* should be called "photonic efficiency" and "apparent quantum efficiency", respectively [31,33]. However, for the sake of simplicity, only *PY* and *AQY* terms are used herein. For gas-phase conditions, the experimental error on H_2 formation rate was evaluated to 10% in standard deviation by testing 4 samples from the same batch (0.2 wt% Pt/TiO_2-P90 pre-reduced at 300 °C). For liquid-phase conditions, it was estimated to 12%.

3. Results

3.1. Structural characterization

A series of 13 samples, listed in Table 2, was investigated, as well as bare TiO_2-P90 and $Pt(NH_3)_4(NO_3)_2$/P90 impregnates (without thermal treatment). The samples are named according to the target loading in wt%Pt, the TiO_2 type, the thermal treatment type, and the maximum temperature in °C. For example, 0.2Pt/P90 C300R300 denotes a catalyst supported on P90, loaded with 0.2 wt% Pt, calcined in air at up to 300 °C, and finally reduced in H_2 at up to 300 °C. The TiO_2 types were commercial P25 and P90, and shape-controlled nanotubes (NT), nanowires (NW) and nanobelts (NB), the main characteristics of which are reported in Table 1.

Table 2. Characteristics of Pt/TiO_2 photocatalysts

Sample	Pt loading (wt%)	Average Pt cluster size (Å)
0.2Pt/P25 R300	0.13	12 ± 3
0.2Pt/P90 C300	0.14	Atomic dispersion
0.2Pt/P90 C300R300	0.12	9 ± 2
0.2Pt/P90 R200	0.11	10 ± 3
0.2Pt/P90 R300	0.13	13 ± 3
0.2Pt/P90 R300C300	0.13	10 ± 3
0.2Pt/P90 R400	0.11	10 ± 3
1Pt/P90 C300	0.58	Atomic dispersion
1Pt/P90 R450	0.75	13 ± 3
1Pt/P90 R600	1.02	16 ± 4
0.2Pt/NT R300	0.19	15 ± 4
0.2Pt/NW R300	0.25	14 ± 3
0.2Pt/NB R300	0.14	17 ± 8

C and R denote calcination and reduction, respectively. NT, NW and NB stand for TiO_2 nanotubes, nanowires and nanobelts, respectively. Pt loadings and average cluster sizes were determined by ICP-OES and STEM, respectively.

While calcination was always performed at 300 °C, reduction was carried out between 200 °C and 600 °C. The minimal temperatures of thermal treatments were chosen on the basis of thermal analysis results, which show that weight loss, heat release and water desorption occur below *ca*. 300 °C for calcination and below *ca*. 200 °C for reduction (Fig. S2).

Figure 1 shows STEM images of the samples, together with the corresponding size histograms. The calcination treatment leads to *ca*. 100% Pt dispersion (*i.e.*, all the Pt atoms are exposed to the surface), with mostly single atoms for 0.2Pt C300 and a mixture of single atoms and small clusters (0.65 ± 0.30 nm) for 1Pt C300. The reduction and calcination-reduction treatments lead to a majority of Pt clusters. For shape-controlled $0.2Pt/TiO_2$ R300, the average Pt cluster size is 1.4-1.7 nm, while it is 1.2 nm for 0.2Pt/P25 and 0.9-1.0 nm for 0.2Pt/P90 samples reduced at up to 400 °C.[b] For the commercial catalysts, the slight decrease in Pt dispersion can be ascribed to the decrease in TiO_2 surface area from P90 (114 m^2/g) to P25 (50 m^2/g). However, this does not hold for shape-controlled anatase titania samples, which exhibit either surface areas higher than 250 m^2/g (nanotubes and nanowires) or small surface area (nanobelts, 35 m^2/g). In those cases, the Pt particle size might also be controlled by the titania texture and surface structure. In particular, nanotubes and nanobelts expose predominantly {100} facets whereas nanowires expose {001} facets [28]. For the P90 support, the Pt loading and the

[b] For 0.2Pt/P90 R300, the size is calculated to be 1.3 ± 0.3 nm, but from 51 particles only (Fig. S9).

reduction temperature were increased to 1 wt% and 450-600 °C, respectively, in order to increase the Pt particle size. As a result, the 1Pt/P90 R450 and 1Pt/P90 R600 samples display average sizes of 1.3 nm and 1.6 nm, respectively. *In situ* X-ray diffraction performed under H_2 flow on a 1 wt% Pt/P90 sample prepared by IWI and direct reduction at 200 °C shows that the titania crystallites start to grow and anatase starts to convert into rutile above 500 °C (Fig. S3). This leads to a loss of surface area, the catalyst treated at 600 °C having a BET surface area of 43 m^2/g. Besides, high-magnification STEM images (Fig. S4) do not reveal the occurrence of strong metal-support interaction (SMSI), i.e. diffusion of titanium oxide over the Pt particles upon reducing thermal treatment at high temperature [34].

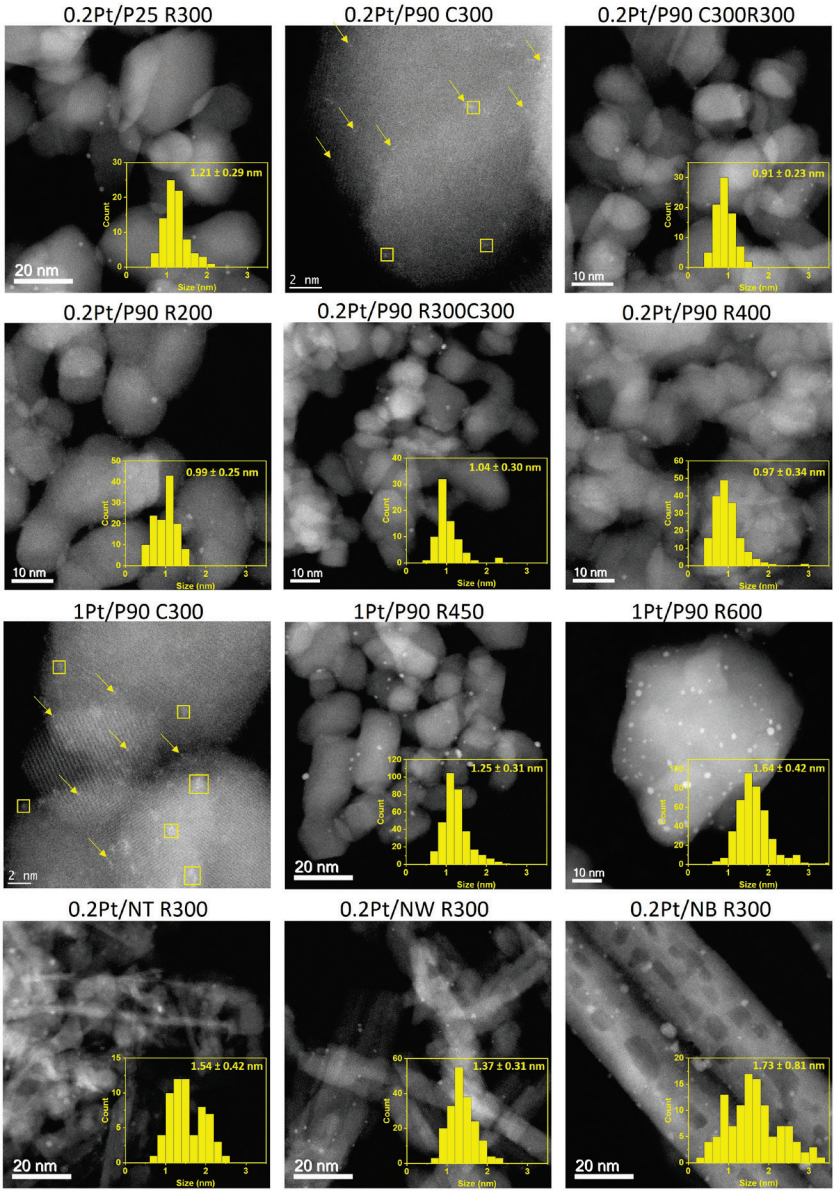

Figure 1. ADF-STEM images and Pt particle size histograms of the as-prepared Pt/TiO_2 samples. The calcined samples contain majority (0.2Pt/P90 C300) and minority (1Pt/P90 C300) fractions of single Pt atoms (arrows), in coexistence with small clusters (squares in 1Pt/P90 C300 image, size 0.65±0.30 nm). NT, NW and NB stand for TiO_2 nanotubes, nanowires and nanobelts, respectively.

3.2. Gas-phase dehydrogenation of ethanol

First, experimental conditions were screened with a given photocatalyst, 0.2Pt/P90 R300. Figures S5 reports the rate of hydrogen production for various catalyst weights and ethanol concentrations in water. Figure S5a shows that the H_2 production rate is roughly constant between 10% and 100% ethanol in the gas phase. Similarly, a previous kinetic study of PHER from water-ethanol mixtures on Au/TiO_2 catalysts has shown that the reaction is near-zero order in ethanol for high ethanol concentrations. This behavior could be well described with a Langmuir-Hinshelwood mechanism [35]. Figure S5b shows that the rate increases with the mass of catalyst, and starts to reach a plateau above *ca*. 2.5 mg, which is due to photon transfer limitations [33,36]. This led us to choose 10% ethanol concentration and 1.8 ± 0.2 mg catalyst weight as standard parameters.

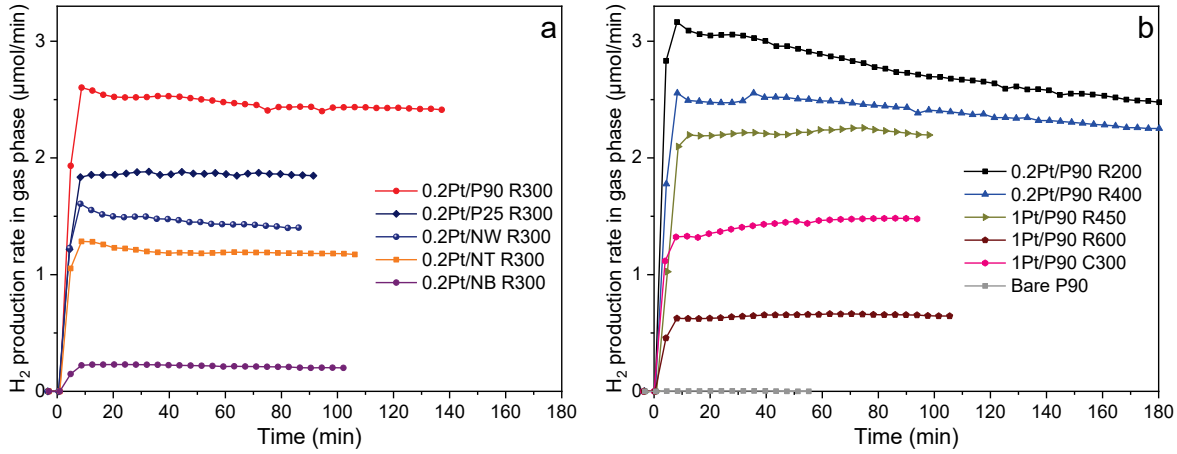

Figure 2. H_2 production rate versus time in gas-phase conditions: (a) effect of TiO_2 type; (b) effect of Pt loading and thermal treatment. The formation of acetaldehyde follows similar kinetics as H_2 formation (not shown).

Figure 2 reports the rate of H_2 production *vs.* time for Pt/TiO_2 catalysts with (a) several TiO_2 types (0.2 wt% Pt, R300) and (b) various thermal treatments (P90, 0.2 or 1 wt% Pt). Figure S6 reports the full dataset, which includes the results for 0.2Pt/P90 C300, C300R300, and R300C300. In addition, a 20 h-long test is shown in Figure S7 for the 0.2Pt/P90 R300 catalyst. In terms of catalytic stability, for the pre-reduced samples, the rate reaches a maximum within 10 min and then stabilizes or slowly decreases. The catalyst treated at the lowest temperature, 0.2Pt/P90 R200, is the one that deactivates most. A different behavior is displayed by the two C300 catalysts, whose rates show an initial induction period (up to 1 h) before stabilization. Thus, low-temperature reduction and/or calcination seem to generate Pt species relatively unstable under the reaction conditions.

From Figure 2a, the activity order between the TiO_2 samples is: NB < NT < NW < P25 < P90. Notably, P90 provides a higher activity than the widely used P25. This trend might relate to the differences in the TiO_2 polymorph phase, the specific surface area and/or the Pt cluster size, and these parameters may influence each other. According to Figure 2b, the pre-calcined catalyst is nearly twice less active than the pre-reduced catalysts (0.2Pt/P90 R200-R400). The highest activities are obtained after reduction in H_2 below 450 °C. For example, in the case of 0.2Pt/P90 R300, the Pt co-catalyst amplification factor with respect to bare TiO_2 reaches 750, which is much higher than previously reported [10,11,21].

Figure S6 shows that, for the 0.2-1 wt% range, the Pt loading has no significant effect on the photocatalytic performance for Pt/P90 C300. This result is consistent with that of Xing *et al*. for Pt supported on anatase or P25 TiO_2 for photocatalytic methanol dehydrogenation. The authors found an increase of the activity with the Pt loading up to 0.2 wt%, followed by a plateau between 0.2 wt% and 1 wt% [37]. For a higher surface-area mesoporous TiO_2 (209 m^2/g against 50 m^2/g for P25), Kandiel *et al.* even evidenced an activity optimum for 0.2 wt% Pt [7]. Alternatively, the above result may be due to the existence of an optimal Pt loading comprised between 0.2 wt% and 1 wt%, as found by Li *et al.* for the same reaction on nanostructured catalysts [21].

Another interesting result (Fig. S6) is that the 0.2Pt/P90 R300C300 has a similar activity as its R300 and C300R300 counterparts, which implies that, for comparable average Pt particles sizes, the initial oxidation state of Pt has little influence on the catalytic activity. Indeed, as compared to reduction, air calcination obviously increases Pt oxidation, but under reaction conditions the same steady active state of Pt appears to be formed for pre-reduced and pre-calcined samples.

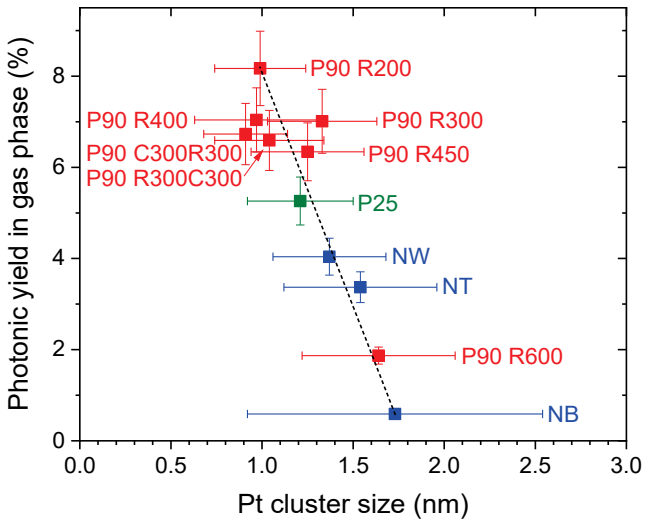

Figure 3. Photonic yield in H_2 after 1 h on stream in gas-phase conditions versus Pt particle size for pre-reduced catalysts. The dotted line is a guide to the eye.

Plotting the photonic yield of H_2 production after 1 h on stream as a function of the Pt cluster size for all the reduced samples suggests an inverse correlation between the photonic yield and the size (Fig. 3). Note that Pt particle size, especially in the range below 2 nm, influences the amount, the geometry, and the electronic structure of surface Pt active sites. As the Pt loading has little effect on the photocatalytic activity, this behavior cannot be ascribed to an influence of the number of available surface Pt sites, and instead points to an intrinsic size effect. The support and the treatment temperature would thus play an indirect role in tuning the Pt cluster size. These results corroborate the recent theoretical investigation by Wang *et al*. predicting that a Pt particle size of 1 nm, corresponding to quasi-bilayer clusters, would be the best compromise between the efficiency of the photoelectron transfer from TiO_2 to Pt (more favorable at smaller sizes) and that of the H-H coupling at the Pt surface (more favorable at larger sizes) [23]. Moreover, our hypothesis on size effect is supported by the results of Li *et al*., who have shown that the crystal facets of TiO_2 do not play a critical role in PHER [17]. However, the Pt/TiO_2 activity might also be influenced by parameters such as the TiO_2 phase and surface area, and the Pt particle shape and number density. In addition, since a reducing treatment at 600 °C initiates TiO_2 modification (Fig. S3) and may also induce SMSI effect (although not evidenced in Fig. S4), the data point for Pt/P90 R600 in Figure 3 should be considered with caution.

While Pt/NB is by far the least active catalyst, Pt/P90 R200 is initially the most active. However, this sample is also the most prone to deactivation (Fig. 2). This may originate from the initially incomplete Pt precursor decomposition, although thermal analysis shows that most features are present below 200 °C (Fig. S2). This led us to test the activity of as-impregnated $Pt(NH_3)_4(NO_3)_2/TiO_2$-P90 (“fresh”) samples. Figure S8 shows that these samples (0.2 wt% and 1 wt% Pt loadings) slowly reach activities similar to that of the 0.2Pt/P90 R300 catalyst. This suggests an autocatalytic process, in which formed H_2 gradually reduces the impregnate. The maximum activities are reached in 26 min and ca. 40 min for 0.2 wt% and 1 wt% Pt loadings, respectively. The activity of the 0.2Pt/P90 fresh sample then slowly decreases (similarly to 0.2Pt/P90 R200), whereas the activity of the 1Pt/P90 fresh sample stabilizes. This difference in behavior recalls that of the two Pt/P90 C300 catalysts (Fig. S6) and may correspond to a two-step process, with Pt reduction followed by agglomeration. The latter likely depends on the Pt loading via the Pt particle surface density.

To explain the differences in time evolution of the H_2 production rates, selected catalysts were analyzed by STEM after the photocatalytic tests. Figure S9 shows representative STEM images and Figure 4 displays the evolution of the Pt particle size histograms from pre- to post-reaction state. The catalysts supported on commercial TiO_2 (P90 and P25) and pre-reduced (R300) exhibit little change:

while in the P90 case the size distribution is almost unaffected, for P25 it shows a positive shift of 0.3 nm. The increase is stronger for 0.2Pt/NT R300, with a positive shift of the average size by 1.0 nm and a broadening of the size distribution by 0.4 nm. Finally, the 1Pt/P90 C300 catalyst, which initially contained a large fraction of single atoms coexisting with subnanometric clusters, is deeply affected by the reaction medium, which mostly generates 2-3 nm-sized nanoparticles. Sintering of Pt species was also observed for 0.2Pt/P90 C300 (Fig. S9). The instability of these pre-oxidized catalysts can be ascribed to photoreduction as well as to the reducing effect of hydrogen, which is known to destabilize metal cations initially anchored on oxides [38–42]. The 0.2Pt/P90 and 1Pt/90 fresh impregnates were also analyzed by STEM after the photocatalytic tests. They exhibit nanoparticles of 2.1 ± 0.4 nm and 1.4 ± 0.4 nm in size, respectively, confirming the *in situ* decomposition of the Pt precursor and the subsequent aggregation of Pt atoms. The larger particle size at lower loading, although counterintuitive, is consistent with the lower activity of the 0.2Pt sample with respect to the 1Pt sample (Fig. S8), when one takes into account the size-activity relationship displayed in Figure 3. Indeed, in spite of the sintering of most catalysts on stream, the inverse correlation between the photonic yield and the Pt particle size is still valid when one considers the post-reaction size, as shown in Figure S10.

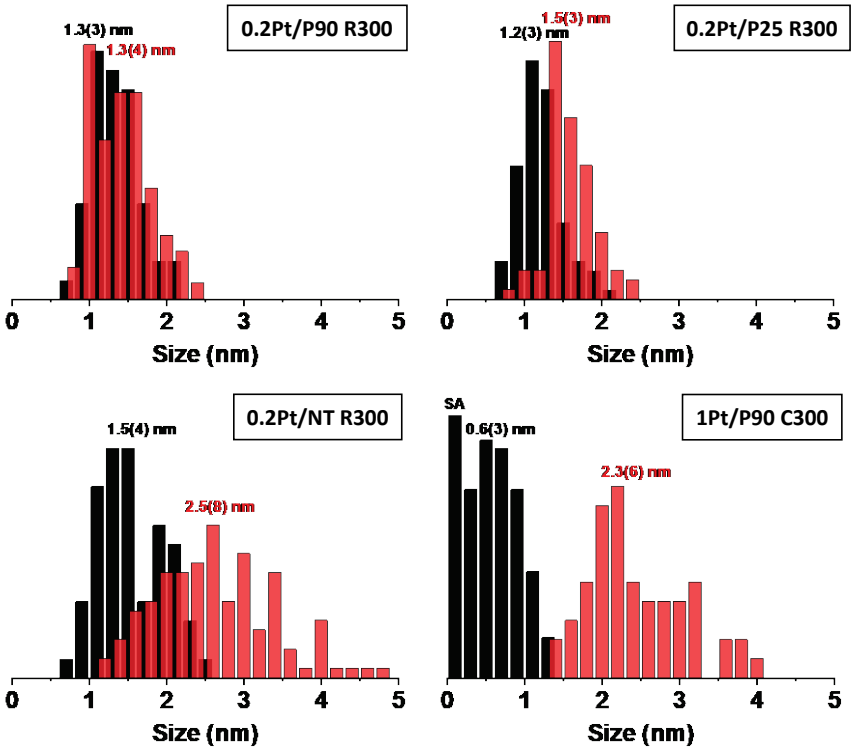

Figure 4. Pt particle size distributions (arbitrary units) determined from STEM before (black) and after (red) the gas-phase catalytic tests. Single atoms and small clusters remaining in 1Pt/P90 C300 after reaction are not taken into account in the corresponding histogram.

3.3. Liquid-phase photocatalytic dehydrogenation of ethanol

In order to confirm the generality of the above results, a selection of the P90-supported catalysts was tested for the same reaction, but in liquid-phase conditions. In this case, the experimental conditions were not screened, but were chosen not to limit the kinetics by the amount of catalyst or ethanol, accordingly to literature works [6,9,13,43].

Figure 5 displays the hydrogen production rate as a function of time. Several observations can be made. For a given Pt loading (0.2 wt%), the activity order is C300 < C300R300 < R300, which is in line with the gas-phase results. More surprising is the effect of the Pt loading, which negatively affects the activity of the C300 catalyst, whereas it has little effect under gas-phase conditions (Fig. 2 and Fig. S6). As pointed out by Li et al., this can be attributed to excessive Pt on TiO_2, which increases the opacity and light scattering of the suspension, thereby reducing the photon absorption of TiO_2. Moreover, Pt at high concentration may act as a charge recombination center, resulting in the decreased activity [21]. The threshold loadings above which these phenomena occur may be different in gaseous and liquid-phase conditions.

Similarly to the gas-phase conditions under which the pre-calcined catalyst activities slowly evolved, in the liquid phase these catalysts show an activation over the whole testing period. This is most likely due to the reduction/aggregation phenomenon previously evoked for the gas phase. Another striking similarity between the two conditions lies in the behavior of the 0.2Pt/P90 and 1Pt/P90 fresh impregnates (see Fig. S11 for liquid phase versus Fig. S8 for gas phase). In both cases, the activities reach their maximum after an induction period, but only 0.2Pt gradually deactivates after reaching its maximum activity, and this activity is lower than that of 1Pt.

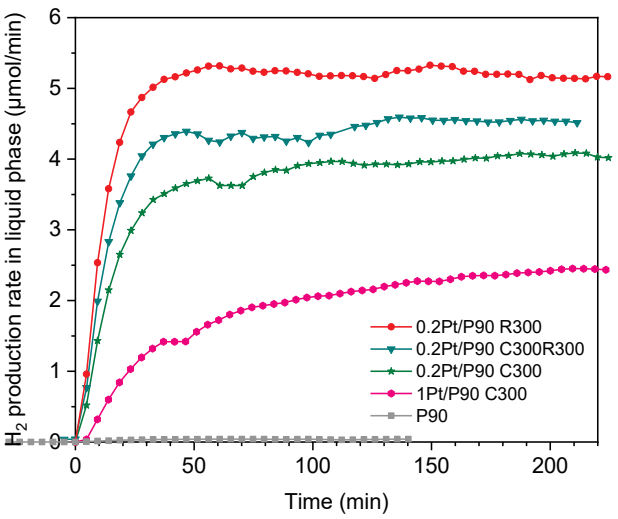

Figure 5. H_2 production rate versus time in liquid-phase conditions for Pt/P90 catalysts.

STEM measurements after the photocatalytic tests show that the Pt particle size in reduced samples is essentially unchanged, whereas again the pre-calcined samples are deeply affected: starting from atomically dispersed Pt, the average Pt particle sizes after the reactions are 2.1 ± 0.4 nm and 2.4 ± 0.6 nm for 0.2Pt/P90 C300 and 1Pt/P90 C300, respectively (Fig. S12). The "fresh" impregnates contain, after the tests, a mixture of Pt species ranging from single Pt atoms to large aggregates (size 2.8 ± 1.1 nm for 0.2Pt/P90 fresh and 11± 4 nm for 1Pt/P90 fresh). Therefore, similarly to gas-phase conditions, in the liquid phase only the reduced catalysts are structurally stable.

3.4. Discussion

Figure 6 reports the photonic yield in liquid phase versus that in gas phase. The 0.2Pt/P90 C300 catalyst, *i.e.* the sample initially composed mainly of single Pt atoms, seems to be favored by liquid-phase conditions. Besides, under our conditions, the co-catalytic effect of Pt with respect to bare TiO_2 is lower in the liquid phase: the maximum ratio between the photonic yields for Pt/TiO_2 and TiO_2 is of 130, versus 960 for 0.2Pt/P90 R200 in the gas phase.

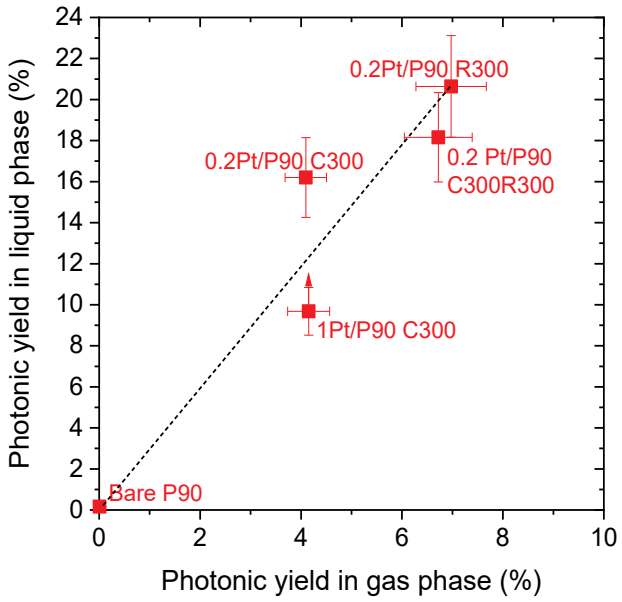

Figure 6. H_2 photonic yield in liquid-phase (after 200 min) versus gas-phase conditions (after 1 h) for Pt/P90 catalysts. The dotted line is a guide to the eye. The vertical arrow indicates the incomplete activation of 1Pt/P90 C300 catalyst (see Fig. 5).

Table 3 summarizes the performances of the 0.2Pt/P90 R300 catalyst in liquid and gaseous phases. The H_2 production rates are of the order or superior to the values reported so far for Pt/TiO_2 catalysts [10,13,16,21,24–26,37,44–46]. Nevertheless, such comparisons should be taken with caution as the experimental conditions (nature of the alcohol, gas or liquid phase, presence of photon-transfer and/or mass-transfer limitations, UV irradiation power, etc.) can have dramatic effects on the photocatalytic activity. Note, however, that the activities of Pt/TiO_2 for PHER from methanol and ethanol aqueous solutions were previously found to be similar [13,19].

Table 3. Performances of the 0.2Pt/P90 R300 catalyst.

Conditions	H_2 prod. rate (µmol/min)	H_2 prod. rate (mmol h^{-1} g_{cat}^{-1})	Photonic yield (%)	App. quantum yield (%)	Co-catalyst factor
Gas phase	2.5	170 [a]	7.0	14	750
Liquid phase	5.2	6.2	21	9.5	130

The co-catalyst factor is the ratio between Pt/TiO_2 and TiO_2 activities measured in the same conditions.
[a] Calculated for 0.5 mg of catalyst (Fig. S5b) to minimize photon-transfer and mass-transfer limitation effects.

4. Conclusions

The focus of this work was on the relationship between the platinum initial state, the Pt cluster size and the resulting PHER activity of the Pt/TiO_2 system. In order to disentangle the effects under investigation from the influence of TiO_2 properties, we studied catalysts supported on several titania types. A series of Pt/TiO_2 photocatalysts was prepared by incipient wetness impregnation of $Pt(NH_3)_4(NO_3)_2$ onto commercial or homemade shape-controlled titania followed by calcination and/or reduction thermal treatments. While calcination-reduction or direct reduction generates Pt clusters of 10-20 Å in size, air calcination leads to atomically dispersed Pt. For the catalysts pre-reduced in H_2, independently of the TiO_2 material, the steady-state gas-phase PHER rate from water-ethanol mixture shows a possible reverse relationship with the Pt cluster size. In particular, the higher surface area of TiO_2-P90 with respect to TiO_2-P25 leads to higher Pt dispersion, which would explain the superior activity in the P90 case. For Pt clusters supported on this form of titania, the Pt loading (0.2 or 1 wt%) and the initial treatment (oxidizing *vs*. reducing) have little influence on the catalytic activity. However, the atomically dispersed catalysts exhibit *ca*. twice less PHER activity than their pre-reduced counterparts. From post-reaction STEM, it appears that the former undergo extensive sintering on stream, whereas cluster catalysts are structurally more stable.

Complementary photocatalytic tests in liquid-phase conditions confirm the superiority of catalysts containing Pt nanoclusters over atomically dispersed Pt. However, pre-calcined low-loaded Pt/TiO_2-

P90, initially containing mostly single Pt atoms, seems favored by liquid-phase conditions. The best performances in both liquid and gas media are obtained with 1 nm-sized Pt clusters supported on TiO_2-P90 (0.2Pt/P90 R300), with H_2 production rates of 170 mmol h^{-1} g_{cat}^{-1} (gas) and 6 mmol h^{-1} g_{cat}^{-1} (liquid).

Acknowledgement

Région Auvergne-Rhône-Alpes (CMIRA 2016 project), Agence Nationale de la Recherche (UltraCat project ANR-17-CE06-0008 and LABEX iMUST ANR-10-LABX-0064/ANR-11-IDEX-0007), MINECO/FEDER ENE2015-63969-R and GC 2017 SGR 128 are acknowledged for financial support. F. Bosselet, P. Mascunan, N. Cristin, and B. Jouguet (IRCELYON) are acknowledged for analyses. The Consortium Lyon-Saint-Etienne de Microscopie (CLYM) is acknowledged for access to the Titan microscope. JL is a Serra Húnter Fellow and is grateful to ICREA Academia program. LM is grateful to CONACYT México for the PhD grant no. 409809.

References

[1] J.H. Montoya, L.C. Seitz, P. Chakthranont, A. Vojvodic, T.F. Jaramillo, J.K. Nørskov, Materials for solar fuels and chemicals, Nat. Mater. 16 (2017) 70–81. doi:10.1038/nmat4778.

[2] K. Takanabe, Photocatalytic Water Splitting: Quantitative Approaches toward Photocatalyst by Design, ACS Catal. 7 (2017) 8006–8022. doi:10.1021/acscatal.7b02662.

[3] D.I. Kondarides, V.M. Daskalaki, A. Patsoura, X.E. Verykios, Hydrogen Production by Photo-Induced Reforming of Biomass Components and Derivatives at Ambient Conditions, Catal. Lett. 122 (2008) 26–32. doi:10.1007/s10562-007-9330-3.

[4] V.M. Daskalaki, D.I. Kondarides, Efficient production of hydrogen by photo-induced reforming of glycerol at ambient conditions, Catal. Today. 144 (2009) 75–80. doi:10.1016/j.cattod.2008.11.009.

[5] M. Murdoch, G.I.N. Waterhouse, M.A. Nadeem, J.B. Metson, M.A. Keane, R.F. Howe, J. Llorca, H. Idriss, The effect of gold loading and particle size on photocatalytic hydrogen production from ethanol over Au/TiO_2 nanoparticles, Nat. Chem. 3 (2011) 489–492. doi:10.1038/nchem.1048.

[6] H. Bahruji, M. Bowker, P.R. Davies, F. Pedrono, New insights into the mechanism of photocatalytic reforming on Pd/TiO_2, Appl. Catal. B. 107 (2011) 205–209. doi:10.1016/j.apcatb.2011.07.015.

[7] T.A. Kandiel, A.A. Ismail, D.W. Bahnemann, Mesoporous TiO_2 nanostructures: a route to minimize Pt loading on titania photocatalysts for hydrogen production, Phys. Chem. Chem. Phys. 13 (2011) 20155–20161. doi:10.1039/C1CP22612F.

[8] T.A. Kandiel, R. Dillert, L. Robben, D.W. Bahnemann, Photonic efficiency and mechanism of photocatalytic molecular hydrogen production over platinized titanium dioxide from aqueous methanol solutions, Catal. Today. 161 (2011) 196–201. doi:10.1016/j.cattod.2010.08.012.

[9] R.M. Navarro, J. Arenales, F. Vaquero, I.D. González, J.L.G. Fierro, The effect of Pt characteristics on the photoactivity of Pt/TiO_2 for hydrogen production from ethanol, Catal. Today. 210 (2013) 33–38. doi:10.1016/j.cattod.2013.01.006.

[10] H. Ahmad, S.K. Kamarudin, L.J. Minggu, M. Kassim, Hydrogen from photo-catalytic water splitting process: A review, Renewable Sustainable Energy Rev. 43 (2015) 599–610. doi:10.1016/j.rser.2014.10.101.

[11] A.V. Puga, Photocatalytic production of hydrogen from biomass-derived feedstocks, Coord. Chem. Rev. 315 (2016) 1–66. doi:10.1016/j.ccr.2015.12.009.

[12] J. Kennedy, H. Bahruji, M. Bowker, P.R. Davies, E. Bouleghlimat, S. Issarapanacheewin, Hydrogen generation by photocatalytic reforming of potential biofuels: Polyols, cyclic alcohols, and saccharides, J. Photochem. Photobiol. A. 356 (2018) 451–456. doi:10.1016/j.jphotochem.2018.01.031.
[13] Z.H.N. Al-Azri, W.-T. Chen, A. Chan, V. Jovic, T. Ina, H. Idriss, G.I.N. Waterhouse, The roles of metal co-catalysts and reaction media in photocatalytic hydrogen production: Performance evaluation of M/TiO_2 photocatalysts (M=Pd, Pt, Au) in different alcohol–water mixtures, J. Catal. 329 (2015) 355–367. doi:10.1016/j.jcat.2015.06.005.
[14] J.M. Herrmann, From catalysis by metals to bifunctional photocatalysis, Top. Catal. 39 (2006) 3–10. doi:10.1007/s11244-006-0032-7.
[15] E. Girel, E. Puzenat, C. Geantet, P. Afanasiev, On the photocatalytic and electrocatalytic hydrogen evolution performance of molybdenum sulfide supported on TiO_2, Catal. Today. 292 (2017) 154–163. doi:10.1016/j.cattod.2016.09.018.
[16] X. Chen, S. Shen, L. Guo, S.S. Mao, Semiconductor-based Photocatalytic Hydrogen Generation, Chem. Rev. 110 (2010) 6503–6570. doi:10.1021/cr1001645.
[17] Y.H. Li, C. Peng, S. Yang, H.F. Wang, H.G. Yang, Critical roles of co-catalysts for molecular hydrogen formation in photocatalysis, J. Catal. 330 (2015) 120–128. doi:10.1016/j.jcat.2015.07.009.
[18] M. Bowker, C. Morton, J. Kennedy, H. Bahruji, J. Greves, W. Jones, P.R. Davies, C. Brookes, P.P. Wells, N. Dimitratos, Hydrogen production by photoreforming of biofuels using Au, Pd and Au–Pd/TiO_2 photocatalysts, J. Catal. 310 (2014) 10–15. doi:10.1016/j.jcat.2013.04.005.
[19] Y.Z. Yang, C.-H. Chang, H. Idriss, Photo-catalytic production of hydrogen form ethanol over M/TiO_2 catalysts (M=Pd, Pt or Rh), Appl. Catal. B. 67 (2006) 217–222. doi:10.1016/j.apcatb.2006.05.007.
[20] E. Bonmatí, A. Casanovas, I. Angurell, J. Llorca, Hydrogen Photoproduction from Ethanol–Water Mixtures Over Au–Cu Alloy Nanoparticles Supported on TiO_2, Top. Catal. 58 (2015) 77–84. doi:10.1007/s11244-014-0347-8.
[21] H. Li, H. Yu, L. Sun, J. Zhai, X. Han, A self-assembled 3D Pt/TiO_2 architecture for high-performance photocatalytic hydrogen production, Nanoscale. 7 (2015) 1610–1615. doi:10.1039/C4NR06310D.
[22] F.F. Schweinberger, M.J. Berr, M. Döblinger, C. Wolff, K.E. Sanwald, A.S. Crampton, C.J. Ridge, F. Jäckel, J. Feldmann, M. Tschurl, U. Heiz, Cluster Size Effects in the Photocatalytic Hydrogen Evolution Reaction, J. Am. Chem. Soc. 135 (2013) 13262–13265. doi:10.1021/ja406070q.
[23] D. Wang, Z.-P. Liu, W.-M. Yang, Revealing the Size Effect of Platinum Cocatalyst for Photocatalytic Hydrogen Evolution on TiO_2 Support: A DFT Study, ACS Catal. 8 (2018) 7270–7278. doi:10.1021/acscatal.8b01886.
[24] J. Xing, H.B. Jiang, J.F. Chen, Y.H. Li, L. Wu, S. Yang, L.R. Zheng, H.F. Wang, P. Hu, H.J. Zhao, H.G. Yang, Active sites on hydrogen evolution photocatalyst, J. Mater. Chem. A. 1 (2013) 15258–15264. doi:10.1039/C3TA13167J.
[25] J. Xing, J.F. Chen, Y.H. Li, W.T. Yuan, Y. Zhou, L.R. Zheng, H.F. Wang, P. Hu, Y. Wang, H.J. Zhao, Y. Wang, H.G. Yang, Stable Isolated Metal Atoms as Active Sites for Photocatalytic Hydrogen Evolution, Chem. Eur. J. 20 (2014) 2138–2144. doi:10.1002/chem.201303366.
[26] Y. Sui, S. Liu, T. Li, Q. Liu, T. Jiang, Y. Guo, J.-L. Luo, Atomically dispersed Pt on specific TiO_2 facets for photocatalytic H_2 evolution, J. Catal. 353 (2017) 250–255. doi:10.1016/j.jcat.2017.07.024.
[27] T. Kasuga, M. Hiramatsu, A. Hoson, T. Sekino, K. Niihara, Formation of Titanium Oxide Nanotube, Langmuir. 14 (1998) 3160–3163. doi:10.1021/la9713816.
[28] L. Martínez, L. Soler, I. Angurell, J. Llorca, Effect of TiO_2 nanoshape on the photoproduction of hydrogen from water-ethanol mixtures over Au_3Cu/TiO_2 prepared with preformed Au-Cu alloy nanoparticles, Appl. Catal. B. (2019). doi:10.1016/j.apcatb.2019.02.053.
[29] E. Molins, M. Benito, I. Mata, L. Martínez, L. Soler, J. Llorca, Au/TiO_2 Lyogels for Hydrogen Production, MRS Adv. 2 (2017) 3499–3504. doi:10.1557/adv.2017.346.
[30] L. Martínez, M. Benito, I. Mata, L. Soler, E. Molins, J. Llorca, Preparation and photocatalytic activity of Au/TiO_2 lyogels for hydrogen production, Sustainable Energy Fuels. 2 (2018) 2284–2295. doi:10.1039/C8SE00293B.
[31] S.E. Braslavsky, A.M. Braun, A.E. Cassano, A.V. Emeline, M.I. Litter, L. Palmisano, V.N. Parmon, N. Serpone, Glossary of terms used in photocatalysis and radiation catalysis (IUPAC Recommendations 2011), Pure Appl. Chem. 83 (2011) 931–1014. doi:10.1351/PAC-REC-09-09-36.
[32] A. Castedo, A. Casanovas, I. Angurell, L. Soler, J. Llorca, Effect of temperature on the gas-phase photocatalytic H_2 generation using microreactors under UVA and sunlight irradiation, Fuel. 222 (2018) 327–333. doi:10.1016/j.fuel.2018.02.128.

[33] M. Qureshi, K. Takanabe, Insights on Measuring and Reporting Heterogeneous Photocatalysis: Efficiency Definitions and Setup Examples, Chem. Mater. 29 (2017) 158–167. doi:10.1021/acs.chemmater.6b02907.
[34] S.J. Tauster, S.C. Fung, R.L. Garten, Strong metal-support interactions. Group 8 noble metals supported on titanium dioxide, J. Am. Chem. Soc. 100 (1978) 170–175. doi:10.1021/ja00469a029.
[35] A. Castedo, I. Uriz, L. Soler, L.M. Gandía, J. Llorca, Kinetic analysis and CFD simulations of the photocatalytic production of hydrogen in silicone microreactors from water-ethanol mixtures, Appl. Catal. B. 203 (2017) 210–217. doi:10.1016/j.apcatb.2016.10.022.
[36] E. Taboada, I. Angurell, J. Llorca, Dynamic photocatalytic hydrogen production from ethanol–water mixtures in an optical fiber honeycomb reactor loaded with Au/TiO_2, J. Catal. 309 (2014) 460–467. doi:10.1016/j.jcat.2013.10.025.
[37] J. Xing, Y.H. Li, H.B. Jiang, Y. Wang, H.G. Yang, The size and valence state effect of Pt on photocatalytic H_2 evolution over platinized TiO_2 photocatalyst, Int. J. Hydrogen Energy. 39 (2014) 1237–1242. doi:10.1016/j.ijhydene.2013.11.041.
[38] W. Sinkler, S.I. Sanchez, S.A. Bradley, J. Wen, B. Mishra, S.D. Kelly, S.R. Bare, Aberration-corrected transmission electron microscopy and in situ XAFS structural characterization of Pt/γ-Al_2O_3 nanoparticles, ChemCatChem. 7 (2015) 3779–3787. doi:10.1002/cctc.201500784.
[39] A.M. Gänzler, M. Casapu, P. Vernoux, S. Loridant, F.J. Cadete Santos Aires, T. Epicier, B. Betz, R. Hoyer, J.-D. Grunwaldt, Tuning the Structure of Platinum Particles on Ceria In Situ for Enhancing the Catalytic Performance of Exhaust Gas Catalysts, Angew. Chem. Int. Ed. 56 (2017) 13078–13082. doi:10.1002/anie.201707842.
[40] L. Liu, D.N. Zakharov, R. Arenal, P. Concepcion, E.A. Stach, A. Corma, Evolution and stabilization of subnanometric metal species in confined space by in situ TEM, Nat. Commun. 9 (2018) 574. doi:10.1038/s41467-018-03012-6.
[41] S. Duan, R. Wang, J. Liu, Stability investigation of a high number density Pt_1 /Fe_2O_3 single-atom catalyst under different gas environments by HAADF-STEM, Nanotechnol. 29 (2018) 204002. doi:10.1088/1361-6528/aab1d2.
[42] C. Dessal, A. Sangnier, C. Chizallet, C. Dujardin, F. Morfin, J.L. Rousset, M. Aouine, M. Bugnet, P. Afanasiev, L. Piccolo, Atmosphere-dependent stability and mobility of Pt single atoms and clusters on γ-Al_2O_3, Nanoscale. in press (2019). doi:10.1039/C9NR01641D.
[43] J.-M. Herrmann, Heterogeneous photocatalysis: state of the art and present applications, Top. Catal. 34 (2005) 49–65. doi:10.1007/s11244-005-3788-2.
[44] B.-S. Huang, F.-Y. Chang, M.-Y. Wey, Photocatalytic properties of redox-treated Pt/TiO_2 photocatalysts for H_2 production from an aqueous methanol solution, Int. J. Hydrogen Energy. 35 (2010) 7699–7705. doi:10.1016/j.ijhydene.2010.05.103.
[45] J. Yu, L. Qi, M. Jaroniec, Hydrogen Production by Photocatalytic Water Splitting over Pt/TiO_2 Nanosheets with Exposed (001) Facets, J. Phys. Chem. C. 114 (2010) 13118–13125. doi:10.1021/jp104488b.
[46] Z. Lian, W. Wang, G. Li, F. Tian, K.S. Schanze, H. Li, Pt-Enhanced Mesoporous Ti^{3+}/TiO_2 with Rapid Bulk to Surface Electron Transfer for Photocatalytic Hydrogen Evolution, ACS Appl. Mater. Interfaces. 9 (2017) 16959–16966. doi:10.1021/acsami.6b11494.